Improving the spectral performance of extended cavity diode lasers using angled-facet laser diode chips

Mandy Krüger[1] · Vasile Z. Tronciu[2] · Ahmad Bawamia[1] · Christian Kürbis[1] · Mindaugas Radziunas[3] · Hans Wenzel[1] · Andreas Wicht[1,4] · Achim Peters[1,4] · Günther Tränkle[1]

Abstract

We present and compare theoretical and experimental results on the electro-optical performance of extended cavity diode lasers (ECDLs) that employ two ridge waveguide designs for the single-transverse mode GaAs laser diode chip. One facet of the laser diode chips serves as a partially reflective output coupler for the laser cavity. The other facet constitutes an intra-cavity interface which introduces spurious optical feedback to the laser diode chip. The waveguide designs differ with respect to the suppression of this spurious feedback. The first design employs a straight ridge waveguide intersecting both facets at normal incidence. The intra-cavity facet is anti-reflection coated and features a residual intensity reflectivity of the order 10^{-4}. The second design employs a bent ridge waveguide intersecting the anti-reflection-coated intra-cavity facet at an appropriate angle. This provides an additional suppression of the spurious intensity reflection to a value estimated to be less than 10^{-6}. We compare the electro-optical performance of both designs theoretically and experimentally. The utilization of a bent waveguide results in an improved spectral stability and purity, specifically a higher side mode suppression and a small intrinsic spectral linewidth over the whole investigated current range, of the external cavity diode laser without sacrificing other parameters such as the output power. The external cavity diode lasers under study exhibit no degradation of the measured frequency noise power spectra and intrinsic linewidths even if there is a drop of the side mode suppression ratio provided that it is not reduced to a very small value. Thus, the usage of a more readily accessible straight waveguide chip in an ECDL could be sufficient if only a limited tuning range and a particularly compact assembly are needed. For spectroscopic applications requiring a small intrinsic spectral linewidth over a large frequency range a bent waveguide chip could be the better choice.

1 Introduction

Owing to their availability over a broad spectral range, their tunability, and their ability to provide excellent spectral stability, diode lasers are best suited for precision spectroscopy applications involving cold atom-based quantum sensors,

e.g., optical atomic clocks or matter-wave interferometers. Furthermore, diode lasers provide compactness, robustness, and energy efficiency which are important aspects for the operation of spectroscopy setups in the field or in space [1–4]. However, the spectral linewidth of monolithic, single longitudinal mode diode lasers such as distributed feedback (DFB) diode lasers or distributed Bragg reflector (DBR) lasers is usually limited to few 100 kHz (full width at half maximum) [5–7]. For cold atom-based applications the laser linewidth often has to be smaller than 100 kHz. Since extended cavity diode lasers (ECDLs) [8, 9] typically meet this requirement, they have become the workhorse for precision quantum optics experiments and devices [10].

However, the coexistence of multiple temporally stable modes is predicted for ECDLs by theory and is also observed experimentally [11, 12]. In case of strongly competing modes, especially in the vicinity of a mode-hop, ECDLs no

✉ Hans Wenzel
   wenzel@fbh-berlin.de

1   Ferdinand-Braun-Institut, Leibniz-Institut für
    Höchstfrequenztechnik, Gustav-Kirchhoff-Str. 4,
    12489 Berlin, Germany

2   Department of Physics, Technical University of Moldova,
    bd. Stefan cel Mare 168, 2004 Chisinau, Moldova

3   Weierstrass Institute, Mohrenstraße 39, 10117 Berlin,
    Germany

4   Institut für Physik, Humboldt-Universität zu Berlin,
    Newtonstr. 1, 12489 Berlin, Germany

longer feature single longitudinal mode emission and thus a small spectral linewidth.

Approaches to improve the stability of single longitudinal mode operation are based on reducing the reflectivity of the external (frequency selective) reflector, on decreasing the residual reflectivity of the intra-cavity laser diode chip facet, or on reducing the optical cavity length of the laser; see Refs. [11, 12].

The latter reduces the form factor and increases the mode-hop-free tuning range. However, the intrinsic linewidth scales with the inverse of the effective cavity length squared, such that the linewidth of the ECDL increases significantly with the reduction of the cavity length [13, 14]. Similarly, a reduction of the reflectivity of the external reflector has a negative impact on the linewidth of the ECDL [13].

In this paper, we theoretically and experimentally investigate the influence of parasitic Fabry–Pérot modes, oscillating between the facets of the laser diode chip, on the spectral stability of ECDLs. We determine and compare the dependence of the emission wavelength, of the side mode suppression ratio (SMSR), and of the frequency noise power spectrum on the injection current for two ECDLs that feature different levels of suppression of these parasitic Fabry–Pérot modes.

The first ECDL (ECDL-1) utilizes a laser diode chip (Chip-1) with a straight ridge waveguide (RW) that intersects both facets at normal incidence; see Fig. 1b. Its front facet is partially reflective so as to act as the resonator output coupler. The rear facet constitutes an intra-cavity interface. This facet is anti-reflection-coated (AR) to reduce its parasitic reflectivity. The second ECDL (ECDL-2) is based on a laser diode chip (Chip-2) with a bent waveguide geometry; see Fig. 1c. Here, as in ECDL-1, the RW intersects the front (output) facet at normal incidence; however, the rear (intra-cavity) facet is intersected at a specific incidence angle [15–18]. This reduces the residual intensity reflectivity of the rear facet of Chip-2 by more than two orders of magnitude with respect to the corresponding reflectivity of Chip-1.

Although the effect of an external feedback on diode lasers has been studied extensively in the past (see e.g., [19, 20]), ECDLs as investigated here are distinguished by the fact that the solitary lasers (i.e., without external feedback) have an extremely high threshold so that they do not work in continuous-wave mode. In Ref. [21] the side mode suppression ratios (SMSRs) of different types of lasers including ECDLs were estimated based on an analysis of the steady-state round-trip conditions for every mode. The derived expression for the SMSR does not account for the non-linear mode interactions taking place above threshold and are thus not able to predict the behavior of ECDLs in dependence on the injection current. The simulations here are based on a time-depended traveling wave model coupled with a rate equation for the carrier density with the results being analyzed using an expansion into the longitudinal modes. We study a special configuration, namely an ECDL with a volume-holographic grating (VHBG) rather than the more common Littrow or Littman–Metcalf designs or filter-based ECDLs, as implemented in our micro-integrated ECDL modules [23].

The paper is organized as follows: The ECDL setup and the laser diode chips are described in Sect. 2. In Sect. 3, calculations of the expected spectral performance based on a traveling wave model are presented for both ECDLs. The experimental results for the two different ECDLs are described in Sect. 4. Finally, the conclusion is given in Sect. 5.

2 ECDL concepts

The laser concept is depicted in Fig. 1a. Both ECDLs consist of a laser diode chip, an intra-cavity lens, and a VHBG. The optical resonator of the ECDLs is formed between the front facet of the laser diode chip and the effective mirror plane of the VHBG. To reduce parasitic compound cavity effects, all optical interfaces within the ECDL resonator are AR coated.

The light emitted from the rear facet of the laser diode chip is imaged into the VHBG (OptiGrate) with an $f = 2.0$ mm aspheric lens (Lightpath 352150-C, $R < 0.5\%$ at both surfaces acc. to specification). The physical length of the various ECDL sections are $l_{VHBG} = 6.7$ mm, $l_1 \approx 1.2$ mm, $l_2 \approx 21.6$ mm, $l_L = 2.0$ mm and $l_{LD} = 2.0$ mm; see Fig. 1a. For this configuration, the free spectral range (FSR) of the laser resonator corresponds to approximately 4 GHz.

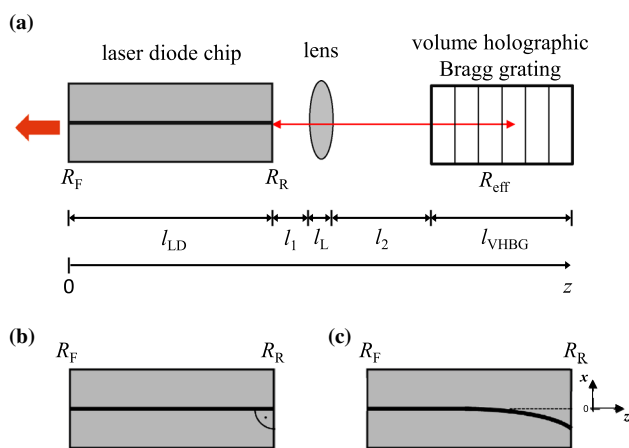The VHBG features a Bragg wavelength of 1064.1 nm, an FWHM bandwidth of 20 GHz, and a resonant

Fig. 1 **a** Schematic of the ECDL concept. **b** Schematic of laser diode chip (Chip-1) with the RW intersecting both facets at normal incidence. **c** Schematic of laser diode chip (Chip-2) with the RW intersecting front (output) facet and rear (intra-cavity) facets at normal incidence and at a specific, non-zero incidence angle, respectively

diffraction efficiency of 70 %. To reduce parasitic feedback from the facets, both facets are AR coated ($R < 0.1 \%$) and tilted by 2.3° from normal to the resonant beam. All specifications are given according to manufacturer. We use the same VHBG for all measurements.

The ECDLs are nominally identical except for the geometry of the RWs chosen for the lateral optical confinement in the $l_{LD} = 2.0$ mm− long laser diode chips. The RW of Chip-1 of ECDL-1 intersects both facets at right angle (incidence angle $\theta = 0°$). Chip-2 of ECDL-2 features a 1.0 mm-long, straight part intersecting the front facet at normal incidence $\theta = 0°$, and of a $l_{bend} = 1.0−$ mm long bent part intersecting the rear facet at an incidence angle of $\theta = 3°$; see Fig. 1c. The lateral displacement $x(z)$ of the RW in the bent section is described by the following expression

$$x(z) = -2l_{bend}\frac{\tan(\theta)}{\pi}\left\{\sin\left[\frac{\pi(z - l_{LD})}{2l_{bend}}\right] + 1\right\}, \tag{1}$$

with $z = [l_{LD} - l_{bend}, l_{LD}]$ denoting the position within the bent section and $z = 0$ indicating the position of the front facet; see Fig. 1a. A comparison between different waveguide bends have been given in [22]. In general, a bend induces two types of optical losses: first, coupling loss between the straight and bent waveguides if the curvature of the bend at the joint is nonvanishing; second, bending loss due to the excitation of radiation modes along the bend. The geometry of the bend according to Eq. (1) gives a compromise between both low coupling and low bending losses if the length of the bend is sufficiently long (depending on the ridge width and height).

The laser diode chips have been fabricated at Ferdinand-Braun-Institut. To reduce the impact of manufacturing tolerances onto the laser performance, both chips were taken from the same wafer, and front and rear facets are partially reflective and AR coated, respectively, together in the same processing runs.

The intensity reflectivity of the front facets has been calculated from the thicknesses and refractive indices of the epitaxial layers and the dielectric layers deposited on the facet, taking into account the RW structure, using the mode matching tool FIMMPROP from Photon Design [24] to $R_F = 29 \%$. The calculated reflectivities of the rear facets are $R_R = 5 \times 10^{-4}$ for Chip-1 and $R_R < 10^{-6}$ for Chip-2. The experimentally determined values of the reflectivities (see Sect. 4) agree quite well with the theoretical values.

The epitaxial layer design was optimized for operation at 1070 nm. The chips feature an InGaAs double quantum well active region with GaAsP barrier and spacers embedded non-centric into AlGaAs based confinement and cladding layers. The large total thickness of the confinement layers of 4.8 μm results in a far field angle of only 15° (full

width at half maximum) which facilitates the beam forming [25]. The width of the ridge of the RW is 5 μm. The difference of the effective refractive indices between the ridge and the etched trench is 3×10^{-3}.

3 Numerical simulations of the ECDLs

Figure 1 depicts the conceptual model of the ECDL, the laser dynamics of which are analyzed in detail in this section. For the numerical simulations of the laser dynamics of ECDL-1 and ECDL-2 the traveling wave model is used [27]. According to this model, the slowly varying complex amplitudes $E^+(z, t)$ and $E^-(z, t)$ of the counter-propagating optical fields within each part of the ECDL are governed by the partial differential equations

$$\frac{n_g}{c_0}\partial_t E^\pm = \left[\mp\partial_z - i\beta(N, I)\right]E^\pm - i\kappa E^\mp + F_{sp}^\pm. \tag{2}$$

Here, ∂_t and ∂_z denote the partial derivatives with respect to time t and longitudinal coordinate z, respectively, n_g is the group index (= 3.66 in the laser diode, 1 in air, 1.6 in the lens, 1.49 in the VHBG), c_0 the speed of light in vacuum, $\kappa = 1.8$ cm^{-1} the field coupling coefficient in the VHBG and $F_{sp}^\pm$ the stochastic spontaneous emission term in the diode laser chip. The relative propagation factor β in Eq. (2) is given by

$$\beta = -i\frac{\alpha(z)}{2} + \delta_T(z, I) + \frac{(i - \alpha_H)g(z, N) - i\mathscr{D}(z)}{2}, \tag{3}$$

with the loss coefficient α (= 2 cm^{-1} in the laser chip, 0 within the VHBG and provides 0.7 field intensity transmission in the gap between the VHBG and the laser diode (to account for the mode coupling efficiency) and the Henry-factor α_H. Self-heating effects in the laser diode are modeled by a linear dependence of the effective index on the injection current $\delta_T(I) = 2\pi n_g\lambda_0^{-2}\nu I$ with $\nu = 1.88$ nm A^{-1} [28]. The nonlinear term $\propto I^2$ due to Joule heating is neglected for simplicity because it would not alter the principal theoretical findings. The function $g(N) = \Gamma g'(N - N_{tr})$ and the operator $\mathscr{D}$ define the carrier-density dependence and the dispersion, respectively, of the modal gain in the laser chip [27]. The optical confinement factor $\Gamma = 0.008$ was calculated from the solution of the optical waveguide equation. Differential gain $g' = 1500 \times 10^{-18}$ cm^2 and transparency carrier density $N_{tr} = 1.4 \times 10^{18}$ cm^{-3} as well as $\alpha_H = 1.2$ were obtained from a microscopic model for the double quantum well active region [26]. Outside the laser chip we set $\mathscr{D} = g' = 0$. The evolution of the carrier density $N(t)$ with time within the laser chip is given by a simple carrier rate equation. Here, we assume a spatially uniform carrier density. As has been shown in [11], the neglect of the variation of the carrier

density due to longitudinal spatial hole burning preserves not only the basic lasing state characteristic (output field intensity, gain in the laser chip, lasing wavelength) at some selected set of parameters, but also the positions of the state transitions when tuning model parameters. More information on the model and parameters can be found in [11, 12, 29].

Finally, we assume that there is no reflection at the facets of the VHBG, whereas at the facets of the diode laser chip the complex fields amplitudes satisfy the following reflection/transmission conditions:

$$E^+(0, t) = -r_F^* E^-(0, t),$$
$$E^-(l_{LD}^-, t) = r_R E^+(l_{LD}^-, t) + t_R E^-(l_{LD}^+, t), \qquad (4)$$
$$E^+(l_{LD}^+, t) = -r_R^* E^-(l_{LD}^+, t) + t_R E^+(l_{LD}^-, t),$$

where l_{LD} denotes the length of the diode laser chip, and l_{LD}^- and l_{LD}^+ denote the same rear facet position inside and outside the diode laser, respectively; refer to Fig. 1. r_F and r_R denote the complex field reflectivity coefficients for the front and rear facets of the diode laser chip, and $t_R = \sqrt{1 - |r_R|^2}$ describes the field transmission coefficient at the rear facet.

The model parameters are the same for both ECDLs except of the field reflectivity coefficient r_R of the rear facet. Whereas for ECDL-1 we account for parasitic reflection at the rear chip facet, $R_R = |r_R|^2 = 5 \times 10^{-4}$, we set $r_R = 0$ for ECDL-2.

Figure 2 shows the electro-optical characteristics simulated for ECDL-1 as a function of the injection current that is swept from smaller to larger values. The thick red curve in Fig. 2a represents the time-averaged output power, P_F, of ECDL-1 transmitted through the front facet of Chip-1. At low injection current settings, ECDL-1 occupies stable stationary states. As the current is increased, unstable operation regimes appear. These are indicated by the thin black and blue curves which show the maximum and minimum instantaneous output power, respectively: within instability regions marked with U, regular periodic undamped oscillations are observed. The scenario how these oscillations are generated and vanish are typical for super-critical and sub-critical, respectively, Hopf bifurcations (bullets D).

Figure 2b shows the time-averaged value of the carrier density.

The behavior of the carrier density differs for currents between 30 and 110 mA and higher currents where unstable regimes appear. For lower currents, the carrier density first decreases and then increases within each region. For higher currents, the carrier density within each stability region first changes with injection current in an oscillatory manner, performing between a half and a full period, and grows monotonically finally. This non-monotonic behavior will be briefly explained below in this section.
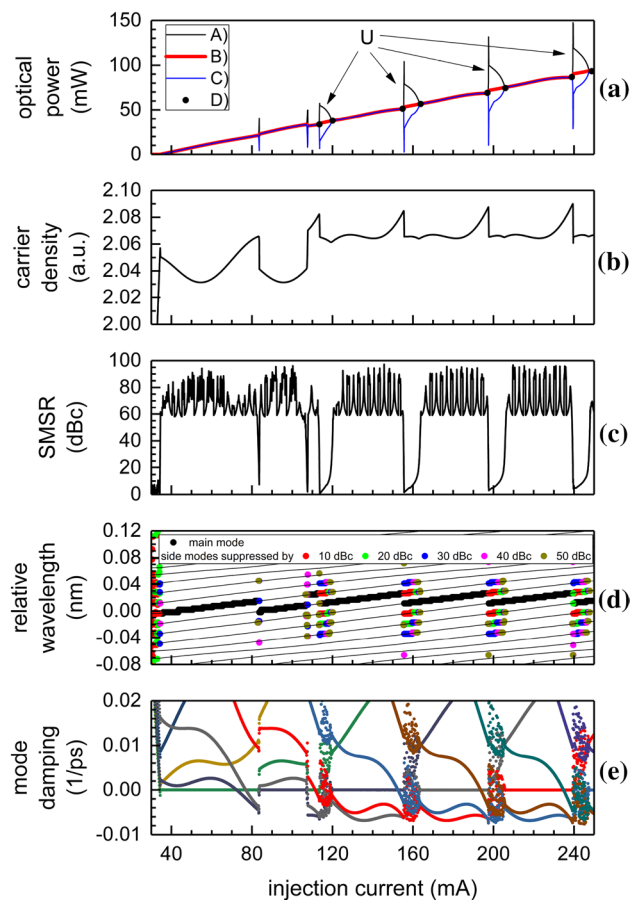
Fig. 2 Electro-optical characteristics simulated for ECDL-1 ($r_R = \sqrt{0.0005}$) as a function of the injection current. Panel **a**: Time-averaged mean B, maximal A and minimal C emission power. Hopf bifurcations D are marked with black bullets. Panel **b**: Time-averaged mean carrier density. Panel **c**: Side mode suppression ratio, as obtained from the Fourier transform [FT]-spectrum. The oscillations are numerical artefacts due to the discrete nature of the FT Panel **d**: Wavelengths of the main peaks of the FT-spectrum (bullets) and modes of the point-spectrum [PS] (thin lines). Big black bullets show the strongest optical mode. The smaller bullets represent the side modes suppressed by less than 10, 20, 30, 40, and 50 dBc, respectively. Panel **e**: Damping of the most important PS modes contributing to the dynamics

To analyze the dependence of the optical spectrum on injection current, we calculate the Fourier transform of the time-trace of the emitted complex field (FT-spectrum) as well as the point spectrum (PS) of the spectral or eigenvalue problem obtained after substituting $E(z, t) = \Theta(N, z)e^{i\Omega(N)t}$ into the field Eqs. (2)–(4) for an instantaneous carrier density N corresponding to the last time moment of simulations for a given injection current. The PS consists of the complex frequencies Ω_k serving as the eigenvalues where k is the index of an optical mode. The real part $Re\Omega_k$ corresponds to the optical frequency of the mode k relative to the reference frequency. In what follows we plot the results in dependence of the relative wavelength $\Delta\lambda = -\lambda_0^2/(2\pi c_0)Re\Omega$,

where $\lambda_0 = 1064$ nm is the reference wavelength. The imaginary parts of the complex frequencies give the damping ($\mathrm{Im}\,\Omega > 0$) or growth ($\mathrm{Im}\,\Omega < 0$) of the optical modes; see Refs. [12] and [30] for more details.

The instability regions in Fig. 2a are correlated with regions of small side mode suppression ratio (SMSR); see Fig. 2c. The SMSR is defined as the ratio between the optical power at the front facet associated with the strongest and the second strongest component of the FT spectrum. The bullets in panel d of Fig. 2 show the wavelengths of several peaks of the FT-spectrum. Here, the size and the color of the bullets represent different levels of side mode suppression. Whereas the full black dots correspond to the strongest mode, the red, green, blue, violet and beige bullets show the side modes suppressed by less than 10, 20, 30, 40 and 50 dB, respectively. The thin curves in the same panel indicate the wavelengths of the optical modes calculated as the PS of the related spectral problem constructed for the last instantaneous value of the carrier density, $N(t)$. This representation provides additional information on the position of the damped modes which, however, can be excited at the bifurcation points either during unstable laser operation or by some external perturbations of control parameters. Deviations between the PS and FT spectra at the wings of the stop-band of the VHBG (relative wavelengths $\approx \pm 0.06$ nm) indicate that four-wave mixing is the origin of the side peaks of the FT spectra.

Finally, panel e of Fig. 2 shows another representation of the PS. The thick lines on the zero damping line, $\mathrm{Im}\,\Omega = 0$, indicate temporally stable lasing of ECDL-1. For small injection current settings, the mode closest to the center of the VHBG stop-band (relative wavelength $\Delta\lambda = 0$) is the mode with the smallest threshold gain. With increasing injection current, the redshift of all modes implies a general but non-monotonic increase of the threshold gain of the dominant mode (see panel b) and simultaneously a general reduction of the threshold gains corresponding to the blue-detuned neighboring side modes once these modes approach the center of the stop-band. Eventually, the two blue-detuned modes closest to the dominant mode exhibit negative damping, $\mathrm{Im}\,\Omega < 0$; see Fig. 2e at $I_{\mathrm{LD}} \approx 72$ mA and $I_{\mathrm{LD}} \approx 78$ mA. Hence, for an instantaneous carrier density these modes can be easily excited, grow, and can determine another possibly temporally stable state with lower carrier density.

The existence of exponentially growing states can be explained by the non-linearity of the whole model including the carrier rate equations. The lasing mode with a sub-optimal threshold does not permit the transition of the field power to the neighboring modes and, therefore, has a non-vanishing basin of attraction in the phase space and can remain stable. However, once the wavelength of the strongest mode is shifted too far from the center of the stop-band of the VHBG, the threshold of this mode becomes too large

and the corresponding state looses its stability. Then, as the injection current is increased further, after some intermediate unstable mode interaction regimes, one of the lower threshold modes becomes the lasing mode. It is interesting to note that at larger injection currents the transition to the adjacent blue-detuned mode rather than to the mode with the smallest threshold is preferred. We argue this mode preference by a better overlap of the adjacent mode profiles (see also Ref. [30]) which is important when exciting neighboring modes. Following the dependence of the mean carrier densities on the injection current shown in Fig. 2b, the (negative) damping of neighboring modes after the state transition changes in an oscillatory manner and remains close to zero. The following bifurcation that leads to the pulsing regime with a significant involvement of three and more modes occurs when the damping of the two closest blue-detuned neighboring side modes become equal and a third blue-side neighboring mode features negative damping, see for example for $I_{\mathrm{LD}} = 115$ mA in panel e of Fig. 2. For more details on the coexistence of several stable steady states in ECDLs determined by different modes at the red stop-band side of the VHBG see Ref. [12].

Figure 3 shows the corresponding characteristics for ECDL-2. In contrast to ECDL-1, this laser features a stable power–current dependence without any instability regions, see Fig. 3a, as well as a large SMSR, see Fig. 3c. Inspection of the small regions corresponding to the state transition in panel d of Fig. 3 shows a nearly complete suppression of the modes which are not directly involved in this transition: red large bullets corresponding to less than 10 dBc side mode suppression are absent in the FT spectrum. The occurrence of FT side peaks in this panel is rather due to a four-wave mixing processes than to excitation of PS side modes through nonlinear mode interaction. The strictly monotonic injection-current dependence of the mean carrier density in Fig. 3b and the main mode damping in Fig. 3e within each stability region also differ from the related changes shown in Fig. 2. We note that once a single mode with $\mathrm{Im}\,\Omega = 0$ determines a temporally stable state, damping of other significant modes changes almost linearly with the change of the injection current. After the damping factors of the two closest blue-detuned neighboring side modes have turned negative, the state transition occurs shortly before or just after these damping factors become equal. The short injection current intervals of comparable negative damping factors as well as the rather different slopes of the damping–current characteristics can be the reason that only one of these modes is significantly involved in the state transition.

For better understanding of the mode analysis discussed above, the correlation between the mode-specific threshold carrier density and the wavelength of different PS modes of ECDL-1 and ECDL-2 are calculated and represented in Fig. 4. In Ref. [12] we have discussed a convenient way to relate the
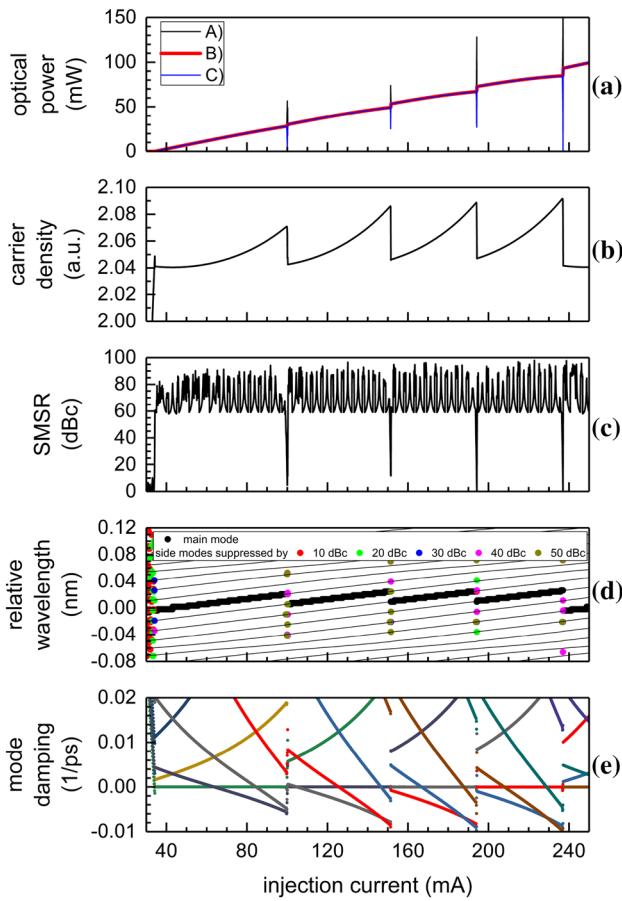
mode-specific threshold carrier density N and relative lasing wavelength $\Delta\lambda$ (proportional to $Re\Omega$) to the field phase shift φ and the attenuation exhibited by the field upon propagation through the external part of the cavity via the round-trip condition [12, 31]

$$\frac{|r_R| + D\,e^{-i(\phi_R - 2\delta_T l_{LD})}}{1 + |r_R|D\,e^{-i(\phi_R - 2\delta_T l_{LD})}}e^{i(\phi_R - \varphi)} = -\eta e^{-2i\Omega\tau_g}r_{eff}, \quad (5)$$

where $D(\Omega, N)$ and $r_{eff}(\Omega)$ denote frequency dependent responses of the laser diode and the VHBG,

$$D(\Omega, N) = \frac{e^{2i\left[\hat{\beta}_{LD}(\Omega,N) + \frac{\Omega n_g}{c_0}\right]l_{LD}}}{r_F^*},$$

$$r_{eff}(\Omega) = \frac{-i\kappa}{\frac{i\Omega n_g}{c_0} + \gamma\cot(l_{VHBG}\,\gamma)}, \quad \gamma = \left(\Omega^2\frac{n_g^2}{c_0^2} - \kappa^2\right)^{1/2},$$
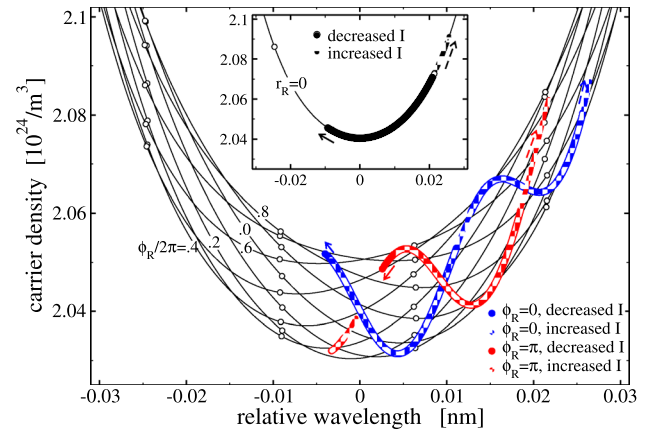

Fig. 4 Steady states in mode wavelength $\Delta\lambda$—carrier density N plane. Thin curves: shift of these states with a change of the field phase factor φ in the air gap part of the ECDL for several fixed values of ϕ_R. Empty bullets: corresponding steady state positions at $\varphi = 0$. Thick blue and red curves: simulated stable steady states for ECDL-1 with $|r_R| = \sqrt{0.0005}$, $\phi_R = 0$ or $\phi_R = \pi$, respectively. Solid and medium thick shaded curve segments represent simulations with an increased and decreased injection current. Insert shows a similar representation of ECDL-2 with $r_R = 0$. All other parameters are the same as in Figs. 2 and 3

and τ_g and η ($= 0.7$ in our case) are the field propagation time in the gap between the diode and the VHBG and the part of the nonscattered field intensity during this propagation, respectively. $\hat{\beta}_{LD}(\Omega, N)$ is a frequency-domain analog of the laser diode propagation factor β given in (3) after excluding the contribution of the thermal detuning δ_T.

In the case when the damping factor of a certain PS mode is $Im\Omega = 0$, this mode defines a steady state of the ECDL.

It can be shown that a nonvanishing complex field reflectivity $r_R = |r_R|e^{i\phi_R}$ strongly affects the wavelength of the PS modes and, therefore, the characteristics of the stationary states. The Eq. (5) for ECDL-1 with $Im\Omega = 0$, $Re\Omega = -2\pi c_0\Delta\lambda/\lambda_0^2$, $|r_R| = \sqrt{0.0005}$, and different values of the roundtrip phase φ in the external cavity are solved for ten different phases $\phi_R = \{0, 0.1, \ldots, 0.9\} \cdot 2\pi$. The result is shown in Fig. 4. The empty bullets represent the (stable or unstable) steady states for fixed $\varphi = 0$. Once tuning the phase factor φ, these steady states move along the curves and replace the adjacent states at $\varphi = 2\pi$ or $\varphi = -2\pi$. Similar single axially symmetric thin curve and empty bullets in the insert of Fig. 4 represent the steady states in ECDL-2 with $r_R = 0$. It is obvious that non-vanishing r_R not only implies an asymmetry of the location of the steady states in the $\Delta\lambda - N$ plane, but also introduces a sensitive dependence of the thresholds of the individual modes on the phase of the rear facet ϕ_R.

Tuning of the injection current I_{LD} in the calculations above has not changed ϕ_R, but modified the factor $\delta_T(I_{LD})$ in the laser chip instead. As a consequence of the left hand

side (lhs) of (5), a change of the thermal detuning $\delta_T(I_{LD})$ in the mode calculations is equivalent to the simultaneous tuning of the effective reflectivity phase, $\phi_{R,eff} = \phi_R - 2\delta_T l_{LD}$, and the field phase, $\varphi_{eff} = \varphi - 2\delta_T l_{LD}$. The presence of such a dual phase tuning is represented by thick curve segments in Fig. 4, which show wavelengths and carrier densities of all stable stationary states obtained during our simulations with decreased (thick solid) and increased (thinner shaded) injection currents. Whereas the blue curves represent the case of $\phi_R = 0$ already discussed in Fig. 2, the red curves correspond to the reflectivity phase $\phi_R = \pi$. In both cases, the steady states along these calculated curves are characterized by oscillatory changes of carrier densities already noticed when discussing Fig. 2b.

Thermal detuning imposed continuous change of the steady states along these curves correspond to the simultaneous change of the effective interface reflectivity phase $\phi_{R,eff}$ (represented by different thin curves) and the effective field tuning factor φ_{eff} (represented by the relative location between two adjacent empty bullets on the corresponding thin curve).

It becomes obvious from this diagram that the reduction of the reflectivity factor $|r_R|$ reduces the separation between the thin (fixed ϕ_R) curves, reduces the amplitude of the carrier density oscillations, and, consequently, makes the performance of the ECDL much more predictable and less dependent on the reflectivity phase. In the case of vanishing reflectivity, $r_R = 0$, the lhs of (5) reads as $D(\Omega, N)e^{i(2\delta_T l_{LD} - \varphi)}$. The resulting equivalence of the thermal detuning and the phase tuning factor is also confirmed by the overlap of the simulated stable steady state locations (thick black segments) with the analytically found thin curve in the insert of Fig. 4.

4 Electro-optical characterization

To determine the residual reflectivity of the rear facet of Chip-1 and Chip-2, both diode laser chips were operated as solitary devices (no feedback from external elements), and the optical power retrieved from the front facet, P_F, and from the rear facet, P_R, was determined as a function of the injection current I_{LD}. The ratio P_F/P_R plotted in Fig. 5 exhibits a strong dependence on the current.

In an unsaturated amplifier, the power ratio is given by [32]

$$\frac{P_F}{P_R} = \frac{1-R_F}{1-R_R} \cdot \frac{1+R_R e^{(g-\alpha)l_{LD}}}{1+R_F e^{(g-\alpha)l_{LD}}}, \tag{6}$$

where g is the modal gain and α is the modal loss. At small currents, $(g-\alpha)l_{LD} \ll 0$ holds and the power ratio is therefore simply given by the ratio of the transmission coefficients
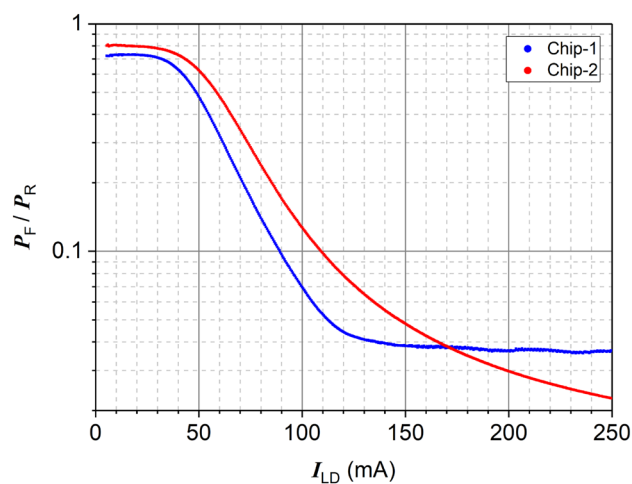

Fig. 5 Comparison of the ratio between the optical power retrieved from the front and rear facet, P_F/P_R, for Chip-1 and Chip-2, both operated as solitary diode lasers

at the facets, $P_F/P_R = (1-R_F)/(1-R_R) \approx (1-R_F)$, as $R_R \ll 1$. Well below transparency the power transmitted through the facets is solely due to (amplified) spontaneous emission created in a volume that is located right behind the corresponding facet and the amount of power impinging onto the facet is hence, for symmetry reasons, the same at the front and rear facets.

Evaluating the data for $I_{LD} \to 0$ we find a front facet transmission of $1 - R_F = 73\%$ and $1 - R_F = 81\%$ for Chip-1 and Chip-2, corresponding to intensity reflectivities of $R_F = 27\%$ and $R_F = 19\%$, respectively. Whereas the first value is close to the calculated theoretical value (29 %), the second one is much smaller. As both chips have been taken from the same wafer and the front facets were coated in the same coating run, we expect the front facets of both chips to feature the same reflectivity. We attribute the difference to measurement inaccuracy.

For higher currents when the chips are operated above transparency, the exponentials in (6) cannot be neglected because the gain g increases with current. The reflectivity at the front facet starts to affect the power output at the rear facet and vice versa. The power ratio decreases monotonically until the laser threshold is reached where the ratio P_F/P_R is independent of the injection current (and output power) and can be described by the Eq. [32]

$$\frac{P_F}{P_R} = \frac{1-R_F}{1-R_R}\sqrt{\frac{R_R}{R_F}}. \tag{7}$$

Chip-1 reaches threshold at $I_{LD} \approx 120\,\text{mA}$ so that it is possible to determine $R_R = 6.9 \cdot 10^{-4}$ from (7) using P_F/P_R at $I_{LD} = 250\,\text{mA}$. This value is near the calculated one

$(5 \cdot 10^{-4})$. Chip-2 does not reach threshold within the accessible current range which indicates a much lower rear-facet reflectivity than Chip-1 as intended.

For the characterization of the electro-optical performance, the ECDL setup is temperature stabilized to $(25.0 \pm 0.5)\,°C$, and the injection current of the laser diode chip is swept up from 30 mA (below laser threshold) to 225 mA. We determine the output power and the SMSR simultaneously for each setting of the injection current.

Due to the small spectral spacing of the ECDL modes (≈ 0.016 nm or 4.2 GHz,) it is impossible to resolve them using an optical spectra analyzer. To determine the SMSR with high resolution (e.g., 3 MHz at 3 dBc, 200 MHz at 50 dBc) we heterodyne therefore the ECDL with a DFB laser (linewidth ≈ 1 MHz full-width-at-half-maximum (FWHM) at 10 ms time scale), detect the corresponding beat note signal with a fast photodetector (New Focus model 1434, 25 GHz bandwidth), and analyze the power
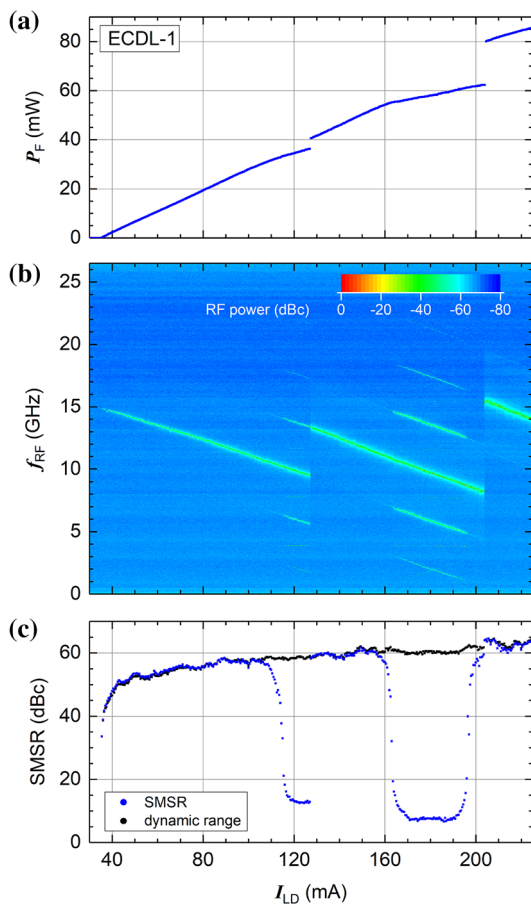

Fig. 6 Experimental results of the electro-optical characterization of ECDL-1. **a** Power–current characteristics. **b** Color map of the RF spectra, derived from the beat note measurement with a DFB laser. All individual RF spectra are commonly normalized to the peak RF power of the map. **c** Side mode suppression ratio (see text)
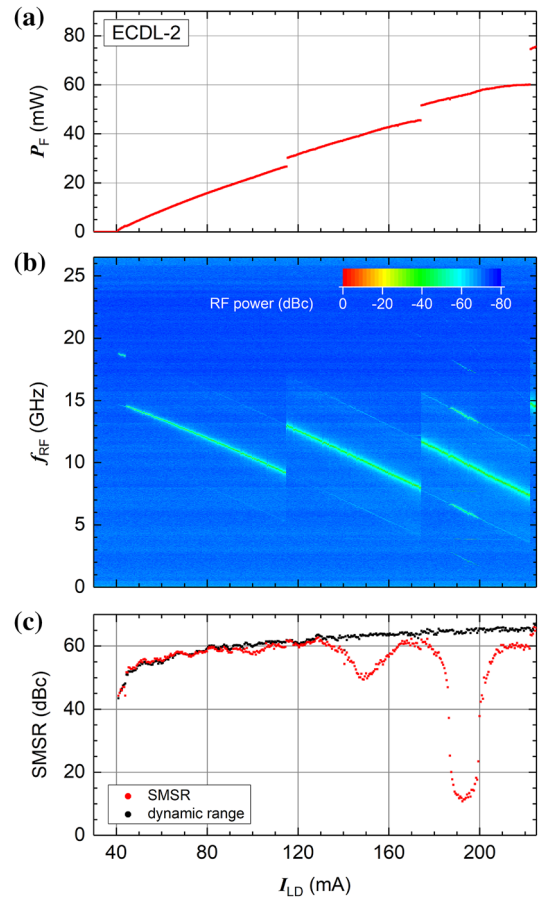

Fig. 7 Experimental results of the electro-optical characterization of ECDL-2. The meaning of all panels is the same as in Fig 6

or radio-frequency (RF) spectrum with an electrical signal analyzer (ESA, Rohde & Schwarz model FSW 26) in spectrum analyzer mode at a resolution bandwidth setting of 3 MHz. In panels a) of Figs. 6 and 7 , the dependence of the optical power P_F on the injection current is depicted. Panels b and c show color maps of the RF spectra and the SMSR, respectively. Both RF spectrum maps are normalized individually to their corresponding peak power. To derive values for the SMSR for each injection current setting, we consider the corresponding RF spectra individually. We determine the SMSR for the two modes adjacent to the strongest mode and calculate the average, i.e., SMSR $= (P_{+1} + P_{-1})/(2 \cdot P_0)$, where P_0 corresponds to the power of the strongest mode and P_{-1} and P_{+1} to the power of the adjacent side modes located one FSR below and above the strongest mode, respectively. The dynamic range of each measurement is limited by the noise floor of the corresponding RF spectrum. It is determined individually for each injection current setting by the ratio between the RF power of the strongest mode and the expected peak RF power of the noise, which is derived from a statistical

analysis of the spectrum taken at $I_{LD} = 30\,\text{mA}$, i.e., below laser threshold. This approach is valid as all settings of the ESA are the same for a given spectrum map and the noise floor is determined by detector and ESA noise rather than laser noise. The dynamic range typically corresponds to values between 50 dBc and 60 dBc.

Both ECDLs feature similar electro-optical performance. According to Figs. 6a and 7a the laser threshold corresponds to about 35 mA and 38 mA for ECDL-1 and ECDL-2, respectively. Further, both ECDLs show several steps in the power–current characteristics. These are correlated to longitudinal mode hops either by one or two longitudinal modes; see the RF spectrum maps in Figs. 6b and 7b. Between mode hops the optical frequency tunes continuously with the injection current for about 5 GHz.

Sweeping up the injection current of both ECDLs from threshold, we find current settings at which the SMSR drops abruptly, within a few mA, to values between 10 dBc and 20 dBc; see Figs. 6c and 7c. As the injection current is swept up further, the SMSR returns to values larger than the dynamic range, again abruptly. The SMSR may be reduced on the verge of a mode hop as well as between two mode hops; see Fig. 6c.

Both ECDLs, however, differ significantly with respect to the smallest injection current, at which the SMSR drops to to values less than 50 dB. Whereas for ECDL-1 the SMSR drops significantly already at an injection current of 110 mA, ECDL-2 has to be operated at an injection current of 190 mA to show the same reduction. Further, the current range for which the SMSR is reduced, is significantly smaller for ECDL-2 than for ECDL-1. We conclude that ECDL-2 is less prone to non-linear interaction of and competition between longitudinal modes than ECDL-1, and attribute this to the fact that parasitic feedback at the rear facet is significantly smaller for ECDL-2 than for ECDL-1.

We next compare the experimental results for ECDL-1 and ECDL-2 to the corresponding simulation results presented in Sect. 3 (see Figs. 2, 3). As detailed below, we find that experimental and theoretical results are in qualitative agreement. Simulations predict a laser threshold of 34 mA for both ECDLs, which is in qualitative agreement with the experimental findings (35 mA for ECDL-1 and 38 mA for ECDL-2).

The simulations further predict mode hops typically every 40– 50 mA for both ECDLs. Whereas for ECDL-2 the experimental result shows mode hops about every 50–60 mA, close to the experiment, the experimental result for ECDL-1 exhibits a hop to the second next mode after a double current period of 80 mA. Such double-mode hops can be also observed in the simulation; see ECDL-2 at a current of 240 mA and [12]. A better agreement could be gained by an adjustment of the thermal detuning δ_T and its current dependence.

For both ECDLs, simulation predicts an abrupt reduction of the SMSR to very small values which is in agreement with the experimental findings. For ECDL-1, the simulation further indicates that strong reduction of the SMSR should occur in the vicinity of a mode hop as well as in between two mode hops; see Fig. 2d at 110 mA. This, again, is in agreement with the experimental findings. However, for ECDL-2, simulation predicts a reduction of the SMSR to only occur in the vicinity of mode hops, while the experiment shows a reduction of the SMSR only in between the mode hops. This discrepancy is attributed to the fact that the simulation for ECDL-2 uses $R_R = 0$, while the true reflectivity is non-zero, i.e., the simulation describes the limiting case of the absence of parasitic feedback from the rear facet while in the experiment parasitic feedback is small but nevertheless present. It should finally be pointed out that both, simulation and experiment, show the current regions of reduced SMSR to be significantly larger for ECDL-1 than for ECDL-2.

In summary, theoretical and experimental findings are in qualitative agreement and show that ECDL-2 is less prone to non-linear interaction of and competition between longitudinal modes than ECDL-1.

Finally, the influence of the ridge waveguide geometry on the frequency noise spectrum and on the intrinsic (Lorentzian) linewidth of the ECDLs is discussed. To determine the frequency noise spectrum, a self-delayed heterodyne (SDH) interferometer with a delay time of $10\,\mu\text{s}$ is used to create an RF beat note signal. The in-phase and quadrature (I and Q) components of this signal are recorded with the ESA for a record length of 100 ms at 100 MS/s with an I / Q signal analysis bandwidth of 80 MHz. The record is split into a number of short sub-records, and the instantaneous phase is determined individually for each sub-record. Next, frequency noise spectra are derived and corrected for the transfer function of the heterodyne interferometer, again individually for each sub-record. Finally, the noise spectra of all sub-records corresponding to the same record are averaged. For Fourier frequencies below (above) 1 MHz, sub-records with a length of 1 ms ($10\,\mu s$) are generated. This approach has been described in detail by Schiemangk et al.; see Ref. [33].

To investigate the frequency stability of the free-running ECDLs, the injection current is swept up from below threshold in steps of $\Delta I_{LD} = 2.5\text{mA}$. Figure 8a shows the corresponding output power P_F as a function of the injection current. For each of the injection current settings, a self-delayed heterodyne beat note measurement is carried out. The intrinsic (Lorentzian) linewidth follows from the single-sided, double-sideband frequency noise power spectral density (FNPSD) $S_f(\nu)$ at sufficiently large Fourier frequencies, where it is white, according to $\Delta f = \pi/2 \cdot \langle S_f(\nu) \rangle_\nu$; see Refs. [33–35] and Fig. 9 for an example. Here, the white noise level is determined by averaging $S_f(\nu)$ between 5 and
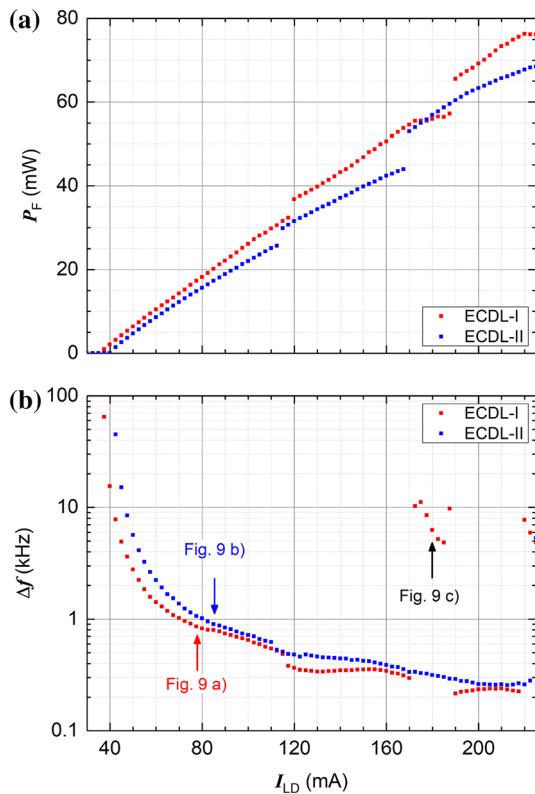
(a)

(b)

Fig. 8 Analysis of frequency instability. **a** Output power P_F of both ECDLs and **b** corresponding intrinsic (Lorentzian) linewidth Δf as a function of the injection current. Optical power and frequency noise data were recorded simultaneously
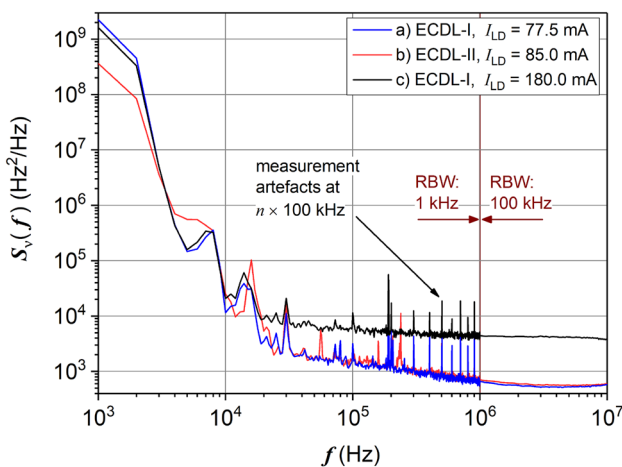

Fig. 9 Single-sided, double-sideband frequency noise power spectral density of the beat note signal derived for **a** ECDL-1 @ I_{LD} = 77.5 mA (red) **b** ECDL-2 @ I_{LD} = 85 mA (blue), both with P_F = 17.3 mW. **c** ECDL-1 @ I_{LD} = 180 mA with P_F = 56.0 mW (black)

10 MHz. The intrinsic linewidth is plotted in Fig. 8b for both ECDLs as a function of the injection current.

We first recognize that the intrinsic linewidths of both ECDLs are similar provided they are operated in a stable regime. However, whereas for ECDL-2 the linewidth basically drops monotonically with increasing injection current, it shows some modulation for ECDL-1, which is attributed to the interaction of the modes due to their coupling through reflection at the rear facet. Further, according to Fig. 8a, ECDL-1 and ECDL-2 feature mode hops between I_{LD} = 117.5 and I_{LD} = 120.0 mA, and between I_{LD} = 112.5 and I_{LD} = 115.0 mA, respectively. No degradation of the intrinsic frequency stability is observed in the vicinity of either of the mode hops. The same applies to the second mode hop of ECDL-2 between I_{LD} = 167.5 and I_{LD} = 170.0 mA. However, it does not apply to the second mode hop of ECDL-1 between I_{LD} = 187.5 and I_{LD} = 190.0 mA. Here, the intrinsic linewidth is increased by a factor of 25 as compared to the linewidth expected for stable operation. The comparison between panels a and b of Fig. 8 suggests that the intrinsic frequency stability is degraded whenever the differential slope dP_F/dI_{LD} drops significantly, e.g., for ECDL-1 between I_{LD} = 170.0 mA and I_{LD} = 190.0 and above I_{LD} = 217.5 mA. With reference to Fig. 6a, b, we recognize that a significant reduction of the differential slope is accompanied by the presence of strong side modes. We finally point out that no degradation of the intrinsic frequency stability is observed for ECDL-2. Again, as already concluded above, this suggests that ECDL-2 is less prone to non-linear interaction of and competition between its longitudinal modes than ECDL-1.

Finally, Fig. 9 shows the FNPSD of the beat note signal for three of the measurements analyzed in Fig. 8. Graphs a (red line) and b (blue line) describe the spectra for ECDL-1 and ECDL-2 at injection current settings of I_{LD} = 77.5 mA and I_{LD} = 85.0 mA, respectively, at which both lasers provide the same output power of P_F = 17.3 mW. Please note that the peaks in the spectra located at integer multiples of 100 kHz are measurement artifacts [33]. Comparison to Figs. 6, 7, and 8 shows that at these operating points no mode hops are in close vicinity and that the SMSR is expected to be large. We find that both spectra are identical within the measurement accuracy and conclude that tilting the waveguide at the rear facet neither improves nor reduces the frequency noise, provided the SMSR is large.

Graph c in Fig. 9 (black line) shows the FNPSD of ECDL-1 operated at I_{LD} = 180 mA, where the SMSR is small; see Fig. 6. Here, the white noise floor corresponds to 4.2×10^3 Hz^2/ Hz. However, at Fourier frequencies below 20 kHz, at which the FNPSD exceeds the white noise level, it is very similar for all three measurements. This suggests that excess frequency noise caused by non-linear mode interaction and mode competition only affects the intrinsic

linewidth. From this, we conclude that thermal effects which could arise from instabilities and feature typical time scales on the order of 1–10 μs are not relevant.

5 Conclusions

In this paper, the influence of parasitic feedback from the intra-cavity facet of a ridge waveguide diode laser chip operated in an ECDL configuration was studied. To this end, two ECDLs operating at 1064 nm were realized, which only differed with respect to the diode laser chips. ECDL-1 employed a diode laser chip with a straight ridge waveguide intersecting both facets at right angle. ECDL-2 employed a diode laser chip with a bent ridge waveguide which intersects the intra-cavity facet at an incidence angle of 3 degrees. Both diode laser chips were taken from the same wafer and feature thus the same InGaAs/GaAsP-AlGaAs double quantum well and fundamental lateral mode ridge waveguide design. Both chips were anti-reflection/partially reflective-coated in the same coating run.

The electro-optical performance of the ECDLs was investigated both theoretically and experimentally. A traveling wave model coupled with a rate equation for the carrier density was used to describe the dynamic behavior of the ECDLs and to predict the dependence of the optical power, averaged carrier density, wavelength, and the side mode suppression ratio in dependence on the injection current. An analysis of the results using an expansion of the computed field into the longitudinal modes has been performed for a better understanding of the different (stable and unstable) regimes of operation. The appearance of several undamped modes having nearly the same negative damping factors are the reason of instabilities (largely reduced for a vanishing intra-cavity reflectivity of the chip facet) and mode hops. The presence of a dual-phase tuning (namely, the tuning of the internal phase of the chip and the external phase of the cavity) results in an oscillatory behavior of the carrier density and the optical power. Simulations revealed that for the device under study the intra-cavity reflectivity must be less than 10^{-5} to eliminate instabilities and oscillations largely. This low reflectivity can be only achieved by tilting the waveguide at the facet of the chip.

In the experiments the output power, the main mode wavelength, the SMSR and the frequency noise power spectrum as well as the intrinsic linewidth were determined as a function of the injection current. Experiments and theory were found to agree qualitatively. Both, the simulation and the experiment, show side modes re-appearing as the injection current is swept up from threshold, with SMSR as small as 10–20 dBc. Reduction of the SMSR was found to be more pronounced for ECDL-1 than for ECDL-2, which is in line with the theoretical predictions and is attributed to the fact that in ECDL-2 the non-linear interaction of the longitudinal modes through parasitic reflection at the intra-cavity chip facet is strongly reduced in comparison to ECDL-1.

Frequency noise power spectra were determined for both lasers experimentally. In the stable operating regimes the two lasers were found to feature similar frequency noise power spectra and intrinsic linewidths. Strong reduction of the SMSR was found experimentally to coincide with operating regimes for which the slope efficiency is strongly reduced. In these regimes the white noise levels of the frequency noise spectra, and hence the intrinsic linewidths, were increased drastically, by a factor of 30. However, the instabilities were found to not affect the frequency noise at small Fourier frequencies (less than 10 kHz) which indicates that thermal effects do not mediate the instabilities.

Surprisingly, both ECDLs exhibit no degradation of the measured frequency noise power spectra and intrinsic linewidths even if there is a drop of the SMSR provided that it is not reduced to a very small value below 10 dB. This enables a stable operation of ECDL-1 over a wider range of currents than expected from theory. Nevertheless, its intrinsic linewidth is deteriorated at certain current ranges due to the appearance of side modes. In contrast, ECDL-2 utilizing a bent-waveguide chip exhibits a low intrinsic linewidth over the whole current range investigated. Thus, if one is interested only in a particular working point, and if this working point can be shifted to a current range (for example, by tuning the current and/or the temperature) where the laser operates stable, a straight-waveguide chip is fine. On the other hand, if a large tuning range is required, e.g., for spectroscopy, a bent-waveguide chip is beneficial. Note that in this case the beam axis is not colinear with the chip axis which could be disadvantageous if a particularly compact assembly is needed.

References

1. T. Lévèque, Rev. Sci. Instrum. **86**, 033104 (2015)
2. K. Bongs, C. R. Phys. **16**, 553–564 (2015)
3. M. Schmidt, A. Senger, M. Hauth, C. Freier, V. Schkolnik, A. Peters, Gyrosc. Navig. **2**, 170–177 (2011)
4. T. Schuldt, Exp. Astron. **39**, 167–206 (2015)
5. S. Spießberger, M. Schiemangk, A. Wicht, H. Wenzel, G. Erbert, G. Tränkle, Appl. Phys. B **104**, 813–818 (2011)
6. T.-P. Nguyen, M. Schiemangk, S. Spießberger, H. Wenzel, A. Wicht, A. Peters, G. Erbert, G. Tränkle, Appl. Phys. B **108**, 767–771 (2012)

7. O. Brox, F. Bugge, A. Mogilatenko, E. Luvsandamdin, A. Wicht, H. Wenzel, G. Erbert, Semicond. Sci. Technol. **29**, 1–6 (2014)
8. C. Wieman, L. Hollberg, Rev. Sci. Instrum. **62**, 1–20 (1991)
9. E.C. Cook, P.J. Martin, T.L. Brown-Heft, J.C. Garman, D.A. Steck, Rev. Sci. Instrum. **83**, 043101 (2012)
10. A.N. Dinkelaker, M. Schiemangk, V. Schkolnik, A. Kenyon, K. Lampmann, A. Wenzlawski, P. Windpassinger, O. Hellmig, T. Wendrich, E.M. Rasel, M. Giunta, C. Deutsch, R. Kürbis, A. Smol, M. Wicht, A.Peters Krutzik, Appl. Opt. **56**, 1388–1396 (2017)
11. V. Tronciu, M. Radziunas, C. Kürbis, H. Wenzel, A. Wicht, Opt. Quant. Electron. **47**, 1459–1464 (2015)
12. M. Radziunas, V.Z. Tronciu, E. Luvsandamdin, C. Kürbis, A. Wicht, H. Wenzel, IEEE J. Quantum Electron. **51**, 2000408 (2015)
13. M.W. Fleming, A. Mooradian, IEEE J. Quantum Electron. **QE–17**, 44–59 (1981)
14. S.D. Saliba, R.E. Scholten, Appl. Opt. **48**, 6961–6966 (2009)
15. C.E. Zah, J.S. Osinski, C. Caneau, S.G. Menocal, L.A. Reith, J. Salzman, F.K. Shokoohi, T.P. Lee, Electron. Lett. **23**, 990–991 (1987)
16. W. Rideout, R. Holmstrom, J. Lacourse, E. Meland, W. Powazinik, Electron. Lett. **26**, 36–37 (1990)
17. A.J. Collar, G.D. Henshall, J. Farré, B. Mikkelsen, Z. Wang, L. Eskildsen, D.S. Olesen, K.E. Stubkjaer, I.E.E.E. Photon, Technol. Lett. **2**, 553–555 (1990)
18. P.J.S. Heim, Z.F. Fan, S.H. Cho, K. Nam, M. Dagenais, F.G. Johnson, R. Leavitt, Electron. Lett. **33**, 1387–1389 (1997)
19. J. Sacher, W. Elsäßer, E.O. Göbel, IEEE J. Quantum Electron. **27**, 373–379 (1991)
20. J. Mork, B. Tromborg, J. Mark, IEEE J. Quantum Electron. **28**, 93–108 (1992)
21. P.W. McIlroy, IEEE J. Quantum Electron. **26**, 991–997 (1990)
22. P.L. Liu, B.J. Li, P.J. Cressman, J.R. Debesis, S. Stoller, I.E.E.E. Photon, Tech. Lett. **3**, 755–756 (1991)
23. A. Wicht, A. Bawamia, M. Krüger, C. Kürbis, M. Schiemangk, R. Smol, A. Peters, G. Tränkle, Proc. SPIE **10085**, 100850F (2017)
24. https://www.photond.com/products/fimmprop.htm. Accessed 28 Mar 2019
25. H. Wenzel, F. Bugge, M. Dallmer, F. Dittmar, J. Fricke, K.H. Hasler, G. Erbert, I.E.E.E. Photon, Tech. Lett. **20**, 214–216 (2008)
26. H. Wenzel, G. Erbert, P.M. Enders, IEEE J. Sel. Top. Quantum Electron. **5**, 637–642 (1999)
27. U. Bandelow, M. Radziunas, J. Sieber, M. Wolfrum, IEEE J. Quantum Electron. **37**, 183–188 (2001)
28. M. Spreemann, M. Lichtner, M. Radziunas, U. Bandelow, H. Wenzel, IEEE J. Quantum Electron. **45**, 609–616 (2009)
29. M. Radziunas, *Handbook of Optoelectronic Device Modeling and Simulation*, 31st edn. (CRC Press, Boca Raton, 2017)
30. M. Radziunas, H.-J. Wünsche, *Optoelectronic Devices* (Springer, New York, 2005), pp. 121–150
31. M. Radziunas, Opt. Quant. Electron. **48**, 470 (2016)
32. H. Wenzel, A. Zeghuzi, *Handbook of Optoelectronic Device Modeling and Simulation*, vol. II, 27th edn. (CRC Press, Boca Raton, 2018)
33. M. Schiemangk, S. Spießberger, A. Wicht, G. Erbert, G. Tränkle, A. Peters, Appl. Opt. **53**, 7138–7143 (2014)
34. G. Di Domenico, S. Schilt, P. Thomann, Appl. Opt. **49**, 4801–4807 (2010)
35. S. Spießberger, M. Schiemangk, A. Sahm, A. Wicht, H. Wenzel, A. Peters, G. Erbert, G. Tränkle, Opt. Express **19**, 7077–7083 (2011)